CHEMISTRY OF MATERIALS

Article

pubs.acs.org/cm

Structural and Electrochemical Consequences of Al and Ga Cosubstitution in $Li_7La_3Zr_2O_{12}$ Solid Electrolytes

Daniel Rettenwander,[*,§] Günther Redhammer,[§] Florian Preishuber-Pflügl,[#] Lei Cheng,[∥,†] Lincoln Miara,[‡] Reinhard Wagner,[§] Andreas Welzl,[⊥] Emmanuelle Suard,[▽] Marca M. Doeff,[∥] Martin Wilkening,[#] Jürgen Fleig,[⊥] and Georg Amthauer[§]

[§]Department of Chemistry and Physics of Materials, University of Salzburg, 5020, Salzburg, Austria

[#]Christian Doppler Laboratory for Lithium Batteries, Institute for Chemistry and Technology of Materials, DFG Research Unit 1277 molife, Graz University of Technology (NAWI Graz), 8010, Graz, Austria

[∥]Lawrence Berkeley National Laboratory, Energy Storage and Distributed Resources Division, University of California, Berkeley, California 94720, United States

[†]Department of Materials Science and Engineering, University of California, Berkeley, 94720, United States

[‡]Samsung Advanced Institute of Technology, 255 Main Street, Cambridge, Massachusetts 02140, United States

[⊥] Institute for Chemical Technologies and Analytics, Vienna University of Technology, 1060 Vienna, Austria

[▽]Diffraction group, Institute Laue-Langevin (ILL), 71 avenue des Martyrs, 38000 Grenoble, France

ABSTRACT: Several "Beyond Li-Ion Battery" concepts such as all solid-state batteries and hybrid liquid/solid systems envision the use of a solid electrolyte to protect Li-metal anodes. These configurations are very attractive due to the possibility of exceptionally high energy densities and high (dis)charge rates, but they are far from being realized practically due to a number of issues including high interfacial resistance and difficulties associated with fabrication. One of the most promising solid electrolyte systems for these applications is Al or Ga stabilized $Li_7La_3Zr_2O_{12}$ (LLZO) based on high ionic conductivities and apparent stability against reduction by Li metal. Nevertheless, the fabrication of dense LLZO membranes with high ionic conductivity and low interfacial resistances remains challenging; it definitely requires a better understanding of the structural and electrochemical properties. In this study, the phase transition from garnet ($Ia\bar{3}d$, No. 230) to "non-garnet" ($I\bar{4}3d$, No. 220) space group as a function of composition and the different sintering behavior of Ga and Al stabilized LLZO are identified as important factors in determining the electrochemical properties. The phase transition was located at an Al:Ga substitution ratio of 0.05:0.15 and is accompanied by a significant lowering of the activation energy for Li-ion transport to 0.26 eV. The phase transition combined with microstructural changes concomitant with an increase of the Ga/Al ratio continuously improves the Li-ion conductivity from 2.6×10^{-4} S cm^{-1} to 1.2×10^{-3} S cm^{-1}, which is close to the calculated maximum for garnet-type materials. The increase in Ga content is also associated with better densification and smaller grains and is accompanied by a change in the area specific resistance (ASR) from 78 to 24 Ω cm^2, the lowest reported value for LLZO so far. These results illustrate that understanding the structure−properties relationships in this class of materials allows practical obstacles to its utilization to be readily overcome.

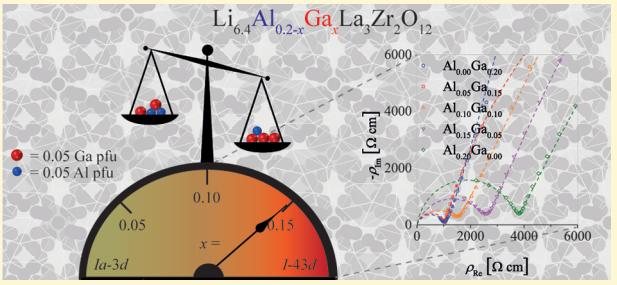

INTRODUCTION

In some "Beyond Li-Ion Battery" concepts, Li metal is used as the anode, e.g., in Li/air, Li/sulfur, and some redox flow batteries.[1] Li metal benefits from a high theoretical specific capacity (3860 mA h g^{-1}), low density (0.59 g cm^3), and the lowest negative electrochemical potential (−3.04 V vs the standard hydrogen electrode) leading to high theoretical energy densities. Nevertheless, safety issues related to the formation of Li dendrites in cells with liquid electrolytes has stymied commercialization of rechargeable high energy batteries with Li-metal anodes. Because of these safety issues, there is renewed interest in the use of solid electrolytes either in all solid-state devices with Li-metal anodes or to protect the Li-metal anodes in a hybrid system that also utilizes a liquid electrolytic solution.[2] Garnets based on $Li_7La_3Zr_2O_{12}$ (LLZO),[3,4] which show high Li-ion conductivities and excellent chemical and electrochemical stability including apparent stability against reduction by Li metal, in particular, are exceptionally well suited for use as a protective layer to enable Li-metal based battery concepts.

Received: February 8, 2016
Revised: March 4, 2016
Published: March 4, 2016

LLZO garnets crystallize in a highly conductive cubic modification (SG: $Ia\bar{3}d$, No. 230)[5] and a less conductive tetragonal polymorph (space group (SG): $I4_1/acd$, No. 142).[6] The former is stabilized at room temperature (RT) by supervalent substitution at the Li, La, or Zr position in LLZO.[7,8] The most promising, and extensively studied, supervalent cations are Al and Ga, generally substituted on the Li sites.[7−9] Much experimental and theoretical effort has been expended to elucidate the site preferences of Al and Ga and their influence on Li-ion dynamics/conduction in LLZO garnets.[10] Additionally, it has been shown that the Li-ion conductivity of LLZO stabilized with Ga is twice that compared to LLZO stabilized with Al.[3,11−17] In order to understand this behavior better, cubic LLZO was synthesized by simultaneous substitution of Al and Ga in different ratios.[10] In the corresponding ^{7}Li NMR line shape measurements an increase in Li-ion dynamics with increasing Ga is observed, as yet the origin of this phenomenon remains, however, unexplained.[10] A possible explanation was found by some recent investigations on single crystals of $Li_{7-3x}Al_xLa_3Zr_2O_{12}$, with x = 0.1−0.4 and $Li_{7-3y}Ga_yLa_3Zr_2O_{12}$, with y = 0.1−0.6 by means of single crystal X-ray diffraction (SC-XRD).[18] It was demonstrated that Ga-stabilized LLZO crystallizes in the acentric "non-garnet" cubic space group $I\bar{4}3d$, No. 220, in contrast to LLZO (see Figure 1 for structural details).[18]

It was shown that the new space group provides a different Li-ion diffusion mechanism leading to faster Li-ion dynamics as shown by NMR relaxometry experiments, recently.[18] The reasons for the phase transition and the relationship to the macroscopic electrochemical properties, such as bulk (σ_{bulk}) and grain boundary (σ_{gb}), Li-ion conductivity, activation energy (E_a), area specific resistance (ASR), and microstructure, were, however, not fully understood.

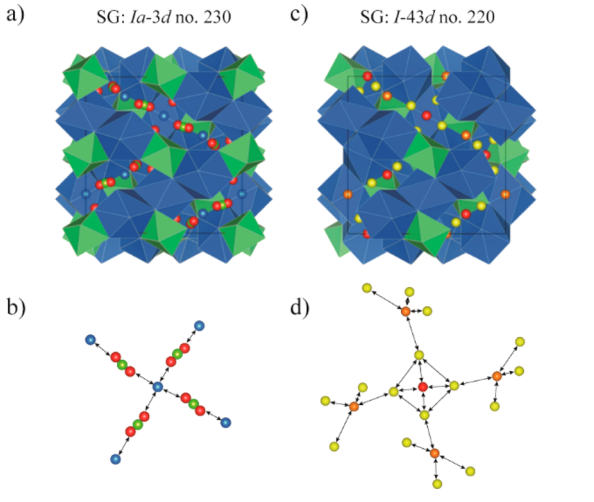

Figure 1. (a) Crystal structure of cubic LLZO with space group $Ia\bar{3}d$ (No. 230). Blue dodecahedra (24*c*) are occupied by La^{3+}, green octahedra (16*a*) by Zr^{4+}. Li^+ are distributed over three sites, viz., tetrahedrally coordinated (24*d*) sites represented by red spheres, octahedrally coordinated (48*g*) sites represented by yellow spheres, and distorted 4-fold coordinated (96*h*) sites represented by orange spheres. The corresponding Li-ion diffusion pathway is shown in (b). (c) Crystal structure of cubic LLZO with space group $I\bar{4}3d$ (No. 220). Blue dodecahedra (24*d*) are occupied by La^{3+}, green octahedra (16*c*) by Zr^{4+}. Li^+ are distributed over three sites, two tetrahedrally coordinated sites 12*a* and 12*b* (equivalent to 24*d* in $Ia\bar{3}d$)) represented by red and orange spheres, respectively, and octahedrally coordinated (48e) sites represented by yellow spheres. The corresponding Li-ion diffusion pathway is shown in (d).

Toward this end, in this work we combine powder X-ray powder diffraction (PXRD), SC-XRD, and neutron powder diffraction (NPD) to characterize samples through simultaneous refinement of the diffraction data. This combination of techniques helped us to obtain a detailed description of the crystal structure. Scanning electron microscopy (SEM) was used to investigate the microstructure as a function of the Al:Ga ratio. Impedance spectroscopy (IS) measurements using both nonblocking electrodes (Li) and blocking electrodes (Til|Pt) covering a wide temperature range (−120 to 40 °C) were used to characterize Li-ion transport and to study solid-state electrochemical properties. Finally, we used density functional theory (DFT) calculations to explain the decrease in activation energy observed with Ga substitution by carefully examining changes in the energy landscape.

We show that, via lattice engineering with Ga substitution at optimized crystallographic sites, the activation energy of ionic conduction can be tailored for higher ionic conduction both in the bulk and at the interfaces.

EXPERIMENTAL SECTION

Synthesis. Synthesis of $Li_{6.4}Al_{0.2-x}Ga_xLa_3Zr_2O_{12}$ garnets, with x = 0.00, 0.05, 0.10, 0.15, and 0.20, was performed by a high-temperature sintering route according ref 18. The starting materials were Li_2CO_3 (99%, Merck), La_2O_3 (99.99%, Aldrich), ZrO_2 (99.0%, Aldrich), Al_2O_3 (99.5%, Aldrich), and Ga_2O_3 (99.0%, Aldrich). Carbonates and oxides in the stoichiometry of the desired composition with a 10% excess of Li_2CO_3 were intimately ground together using a hand mortar, a pestle, and isopropanol. This mixture was pressed uniaxially to form pellets, placed into a corundum crucible, and heated to 850 °C for 4 h with a heating rate of 5 °C/min. To avoid undesired contamination with Al from the crucible, the samples were placed on a pellet of pure LLZO. Afterward the furnace was shut down and the sample allowed to cool down naturally in the furnace to approximately 200 °C. For the second and final step, the samples were milled in isopropanol in a Fritsch Pulverisette 7 ball mill for 2 h (12 times 800 rpm for 5 min + 5 min break). Finally, the powder was isostatically pressed (24 kbar) to form pellets and sintered at 1230 °C for 6 h, with a heating rate of 20.5 °C/min, and were allowed to cool down to RT. To avoid incorporation of Al^{3+} from the crucible, the samples were again placed on a pellet of pure LLZO. To suppress formation of extra phases due to Li loss during sintering, the sample pellets were covered with a pellet of pure LLZO. After synthesis, samples were immediately packed under argon to avoid any contact with moisture from the air (for SC-XRD measurements only).

PXRD. PXRD measurements were performed on powders from the crushed pellets used for SC-XRD with a Bruker D8 DaVinci Design diffractometer (280 mm goniometer radius, Lynxeye solid state detector, primary and secondary side Soller slits, Cu Kα radiation, collection range 10−120° 2θ). For lattice parameter refinements using the program TOPAS V2.1 (Bruker AXS), phase pure material was mixed with silicon as an internal standard (a = 5.43088 Å). For PXRD studies the remaining samples used for SCXRD were used.

SC-XRD. SC-XRD data were collected on a Bruker SMART APEX CCD - diffractometer using Mo Kα radiation. Small single crystals up to 150 μm were selected from the crushed pellets after synthesis and sealed into glass capillaries to avoid prolonged exposure to humidity. Intensity data were collected on samples within 48 h of their synthesis, using graphite-monochromatized Mo Kα X-radiation (50 kV, 30 mA). The crystal-to-detector distance was 30 mm, and the detector was positioned at −30° and (for some points) at −50° 2θ using an ω-scan mode strategy at four different ϕ positions (0°, 90°, 180°, and 270°) for each 2θ position. 630 frames with $\Delta\omega$ = 0.3° were acquired for each run. With this strategy, data in a large Q-range up to minimum d-values d = 0.53 Å could be acquired. Three dimensional data were

DOI: 10.1021/acs.chemmater.6b00579
Chem. Mater. 2016, 28, 2384−2392

integrated and corrected for Lorentz, polarization, and background effects using the APEX2 software (Bruker, 2012).[19] Structure solution (using direct methods) and subsequent weighted full-matrix least-squares refinements on F^2 were done with SHELX-2012 (Sheldrick, 2008) as implemented in the program suite WinGX 2014.1 (Farrugia, 2012).[20,21] Several crystallographic positions show a mixed occupancy with Li^+, Al^{3+}, and Ga^{3+} and vacancies. To overcome this ambiguity, special restrains were chosen: For the Ga^{3+} rich samples with space group $I\bar{4}3d$, Al^{3+} was put onto the 12*a* position, while Ga^{3+} was allowed to distribute over 12*a* and 12*b* positions, together with Li^+; assuming full occupancy of 12*a* and 12*b* sites yields slightly to low Ga^{3+} contents, so vacancies were introduced until the refined Ga^{3+} content met the one obtained from EDX analysis. A similar approach was used for samples with SG $Ia\bar{3}d$; however, here the Ga^{3+} and Al^{3+} were directly fixed onto 24*d* positions while the Li^+ content was freely refined. More details on single crystal structure refinements can be obtained from CIFs with CSD numbers: 430571 (LLZO:$Al_{0.20}Ga_{0.00}$), 430574 (LLZO:$Al_{0.15}Ga_{0.05}$), 430575 (LLZO:$Al_{0.10}Ga_{0.10}$), 430576 (LLZO:$Al_{0.05}Ga_{0.15}$), and 430603 (LLZO:$Al_{0.00}Ga_{0.15}$).

The densities of pellets are calculated from the diameter, thickness, and weight of the obtained pellets. Theoretical densities of pellets are calculated from the cell parameters from the SC-XRD measurement.

NPD. The remaining samples used for SC-XRD were ground and used for NPD studies. The neutron diffraction experiments were done at the Institut Laue-Langevin, ILL, in Grenoble (France). Powder diffraction data were acquired in constant wavelength mode (λ = 1.5441 Å) using the D20 diffractometer on ∼5 g batches contained in 14 mm diameter vanadium sample cans at 298 K. Experiments were performed in the range $5.8° \leq 2\theta \leq 159.7°$, step width 0.04°. An absorption correction was applied to the neutron diffraction data.[22] Data treatment and refinement was done using the FULLPROF-suite of programs.[6] The Thompson−Cox−Hastings pseudo-Voigt function corrected for axial divergence, in conjunction with the D20 resolution function, was used to model peak shape. After satisfactorily refinement of neutron powder and SC-XRD data, the both data sets were joined together, and simultaneous refinements were performed, the results are discussed in text and tables. During mixed refinement, the Ga^{3+} content (when present) was fixed to the value obtained from EDX analysis for all refinements, while the Li^+ and Al^{3+} content was allowed to freely refine for the $Ia\bar{3}d$ structure. For sample LLZO:$Al_{0.05}Ga_{0.15}$, both the Ga^{3+} and Al^{3+} contents were fixed to the EDX values, assuming that they occupy the Li1 site only as evidenced from SC-XRD data, while the Li^+ content was allowed to adjust unconstrained. For sample LLZO:$Al_{0.00}Ga_{0.20}$ a similar strategy was applied. No stable refinements could be achieved putting Al^{3+} or Ga^{3+} onto the interstitial Li3 site.

SEM. SEM images were taken using a Zeiss Ultra Plus device. In particular, we put emphasis on the investigation of the grain size, morphology, and phase composition, and the Al and Ga content using a backscattered electrons detector (BSE) and energy-dispersive X-ray spectroscopy (EDX) measurements, respectively.

IS. IS (impedance spectroscopy) measurements were carried out to investigate Li-ion conductivities. Pt thin films were sputter deposited with a thickness of 200 nm on top of ca. 10 nm Ti (used to improve the adhesion between the sample and the electrode). For the IS measurements a Novocontrol Alpha analyzer was used in the frequency range of 3×10^6 to 10^1 Hz. A Julabo F-25 HE circulator was used for cooling and partly also heating the samples under investigation. Set temperatures between −12 and 25 °C (partly 40 °C) were used, leading to true sample temperatures from ca. −8 to 36 °C. In the following, true sample temperatures, measured by a thermocouple, are indicated in all diagrams. An additional impedance spectrum was recorded for a Li/garnet/Li sample at room temperature in an Ar glovebox. For this, metallic lithium was first applied on the surfaces of the pellet, and the pellet was sandwiched with two lithium foil disks in a Swagelok type cell.[23] Impedance data down to −120 °C were recorded with a Novocontrol Concept 80 spectrometer that is connected to a Quatro cryo system and equipped with a ZGS active sample cell (Novocontrol).

DFT. A single Ga^{3+} or Al^{3+} ion was placed onto the 24*d* site of the $Ia\bar{3}d$ crystal structure with parameters taken from SC-XRD measurements, and then an enumeration algorithm was used to generate structures with one Li placed into each of the distinct remaining sites (i.e., 24*d*, and 96*h*).[24] Total energy calculations were performed in the Perdew−Burke−Ernzerhof (PBE) generalized-gradient approximation (GGA), implemented in the Vienna Ab initio Simulation Package (VASP).[25,26] The projector augmented-wave (PAW) method is used for representation of core states.[27] An energy cutoff of 520 eV and a *k*-point density of at least 1000/(number of atoms in the unit cell) was used for all computations, with a background charge added to compensate for the lack of Li. During the relaxation the structures with the Li in an octahedral site always relaxed to the nearest tetrahedral site in good agreement with previous calculations.[28] The total energy difference between structures with Li in the tetrahedral site closest to and farthest from the supervalent cation was calculated (see below).

RESULTS AND DISCUSSION

For the sake of simplicity, samples with formula $Li_{6.4}Al_{0.2-x}Ga_xLa_3Zr_2O_{12}$ are denoted LLZO:$Al_{0.20-x}Ga_x$. First, the microstructure as a function of the Al:Ga ratio was investigated. Back scattered electron (BSE)−SEM micrographs of the polished pellets are shown in Figure 2. Since BSE is

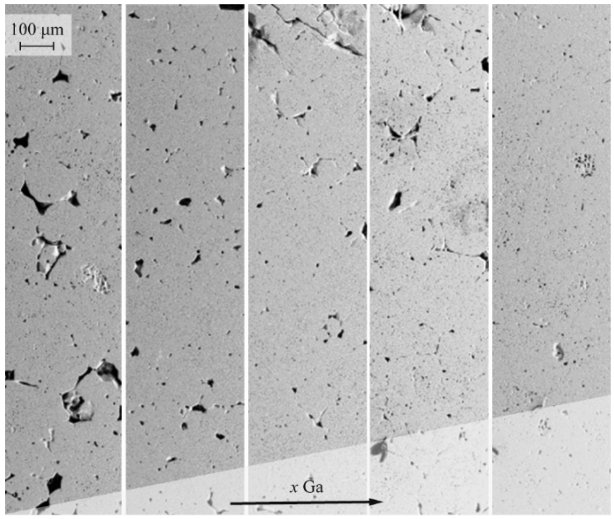

Figure 2. BSE-SEM image of polished embedded pellets of $Li_{6.4}Al_{0.2-x}Ga_xLa_3Zr_2O_{12}$; from left to right, x = 0.00, 0.05, 0.10, 0.15, and 0.20.

sensitive to the atomic number, phases with different compositions can be easily distinguished. No composition other than LLZO was observed, which is in agreement with PXRD and NPD data. The increase of Ga in LLZO:$Al_{0.20-x}Ga_x$ is correlated with a denser studded microstructure with better connected grains and smaller pores. In contrast, the increase of Al leads simultaneously to more pronounced separation of grains and increased grain sizes (up to 200−300 μm). The relative theoretical density for all samples is, however, almost the same and amounts to 85.0(3)%. The Al and Ga content (Al:Ga) of $Li_{6.4}Al_{0.2-x}Ga_xLa_3Zr_2O_{12}$, with x = 0.00, 0.05, 0.10, 0.15, and 0.20, measured by EDX is 0.19:0.00, 0.14:0.05, 0.12:0.08, 0.07:0.14, and 0.00:0.21, respectively (see also Table 1).

Polycrystalline samples of LLZO:$Al_{0.20-x}Ga_x$ with x = 0.00−0.20 were obtained from the pellets and used for the structure determination (XRD, SC-XRD, NPD). Analysis of systematic extinctions of Bragg peaks in the single crystal data sets of the

DOI: 10.1021/acs.chemmater.6b00579
Chem. Mater. 2016, 28, 2384−2392

Table 1. Basic Structural Data and Cationic Distribution of LLZO:$Al_{0.20-x}Ga_x$ Garnets As Determined from Simultaneous Refinement of Powder Neutron Diffraction and Single Crystal X-ray Diffraction Data[a]

	x = 0.00	x = 0.05	x = 0.10	x = 0.15	x = 0.20
SG	$Ia\bar{3}d$	$Ia\bar{3}d$	$Ia\bar{3}d$	$I\bar{4}3d$	$I\bar{4}3d$
a_0	12.9894(2)	12.9892(2)	12.9905(2)	12.9941(2)	12.9936(2)
Li_{24d}	1.606(4)	1.706(11)	2.01(2)	1.01(2)	1.11(3)
$\rightarrow_{12a/b}$				1.23(2)	1.31(2)
Al_{24d}	0.191(8)	0.198(18)	0.118(14)	0.070(14)	-
$\rightarrow_{12a/b}$				-	-
Ga_{24d}	-	0.048[b]	0.080[b]	0.140[b]	0.21(2)
$\rightarrow_{12a/b}$				-	-
$\square_{24d}$	1.203	1.048	0.789	0.284	0.180
$\rightarrow_{12a/b}$				0.268	0.187
$Li_{96h}\rightarrow_{48e}$	3.750(8)	3.668(11)	4.219(9)	3.03(3)	4.38(2)
$\square_{96h}\rightarrow\square_{48e}$	0.801	0.907	1.190	1.504	1.623
Li_{sum}	6.805	6.800	6.828	6.734	6.799
$\square_{sum}$	2.004	1.955	1.974	1.772	1.810
La	2.937(10)	2.947(10)	2.935(10)	2.885(11)	2.951(11)
Zr	2.000[b]	2.000[b]	2.000[b]	2.000[b]	2.000[b]

[a]Lattice parameter a_0 is given in Å; site occupation values in atoms per formula unit (pfu). [b]Fixed values, obtained by EDX.

Al-rich compositions unambiguously yield the common garnet space group $Ia\bar{3}d$ for LLZO:$Al_{0.20}Ga_{0.00}$, LLZO:$Al_{0.15}Ga_{0.05}$, and LLZO:$Al_{0.10}Ga_{0.10}$. For compositions LLZO:$Al_{0.05}Ga_{0.15}$ and LLZO:$Al_{0.00}Ga_{0.20}$, the acentric space group $I\bar{4}3d$ was observed as described in detail by Wagner et al. (2016), recently.[18] Basic structural data are compiled in Table 1. The Li-ion distribution as well as the lattice parameter as a function of the proportion of Ga is illustrated in Figure 3.

On the basis of single crystal structure refinements of samples synthesized under the specific conditions as set out in the Experimental Section it is assumed that in SG $Ia\bar{3}d$ Al and Ga is enriched on the tetrahedral 24*d* sites in LLZO; the 16*a* site is fully occupied by Zr^{4+}, and the 24*c* site contains La^{3+} and a small amount of vacancies. With increasing Ga content the amount of vacancies on 24*c* tends to decrease; there is, however, no clear picture from XRD data. In combined refinements, this tendency of decreasing vacancies is tentatively supported. For Ga^{3+} content > 0.10 pfu a change in space group symmetry to $I\bar{4}3d$ is observed. For the latter SG there is strong evidence that Ga and Al are enriched onto the tetrahedral 12*a* site; this is observed in both single crystal X-ray diffraction and data from combined refinement (SC-XRD and NPD) and supported by DFT calculations. The concentration of vacancies seems to be lower on 12*a* and 12*b* sites in $I\bar{4}3d$ SG as compared to $Ia\bar{3}d$. In addition to the tetrahedral site(s), Li is also found on 96*h* and 48*e* positions, respectively. Combined refinements seem to slightly overestimate the amount of Li on these sites. Consequently, the overall content of Li is right above the ideal value of ~6.40 pfu for 0.20 pfu trivalent cations substituted. However, considering the lower La content (according to simultaneous refinement of diffraction data), the Li content is in good agreement according charge neutrality. Moreover, an increase of Li occupation at the 24*d* site is observed. This behavior was suggested to be responsible for the decrease in electrochemical performance.[4] In the present study, however, electrochemical properties seem to be improved by the Li occupation behavior observed (see below).

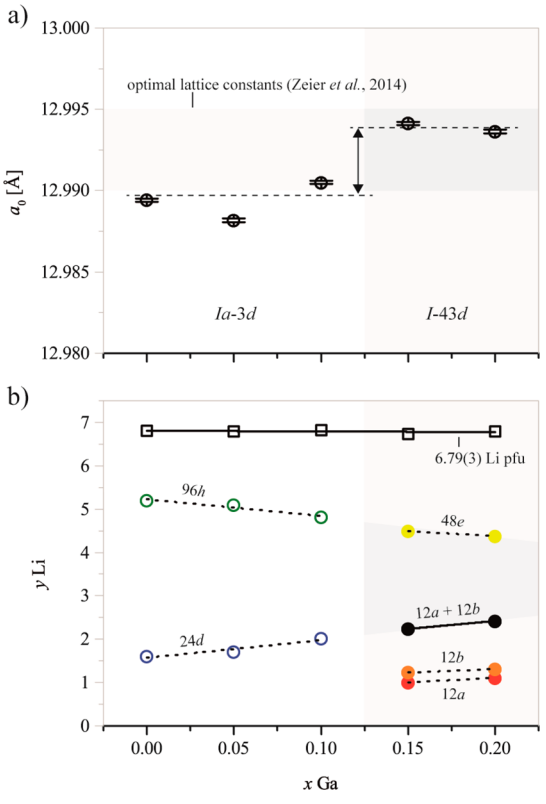

Figure 3. Lattice parameter (a_0) (a) and Li site distribution (b) in $Li_{6.4}Al_{0.2-x}Ga_xLa_3Zr_2O_{12}$, with x = 0.00, 0.05, 0.10, 0.15, and 0.20.

The replacement of Al^{3+} by Ga^{3+} slightly increases the lattice parameter a_0, and this finding is evident from the single crystal data. The change of symmetry, however, is not well pronounced in the variation of lattice parameters within the compositions.

In order to investigate the influence of space group and microstructure on σ_b, σ_{gb}, and E_a, impedance spectra were measured using blocking electrodes (Ti|Pt) for all compositions at temperatures between −120 and 40 °C. Figure 4 displays the results, measured at 20, and −80 °C.

At 20 °C, all samples show a more or less complete high frequency semicircle followed by a strong increase of the imaginary part of the impedance toward low frequencies with an almost constant angle in the complex impedance plane. As

DOI: 10.1021/acs.chemmater.6b00579
Chem. Mater. 2016, 28, 2384−2392

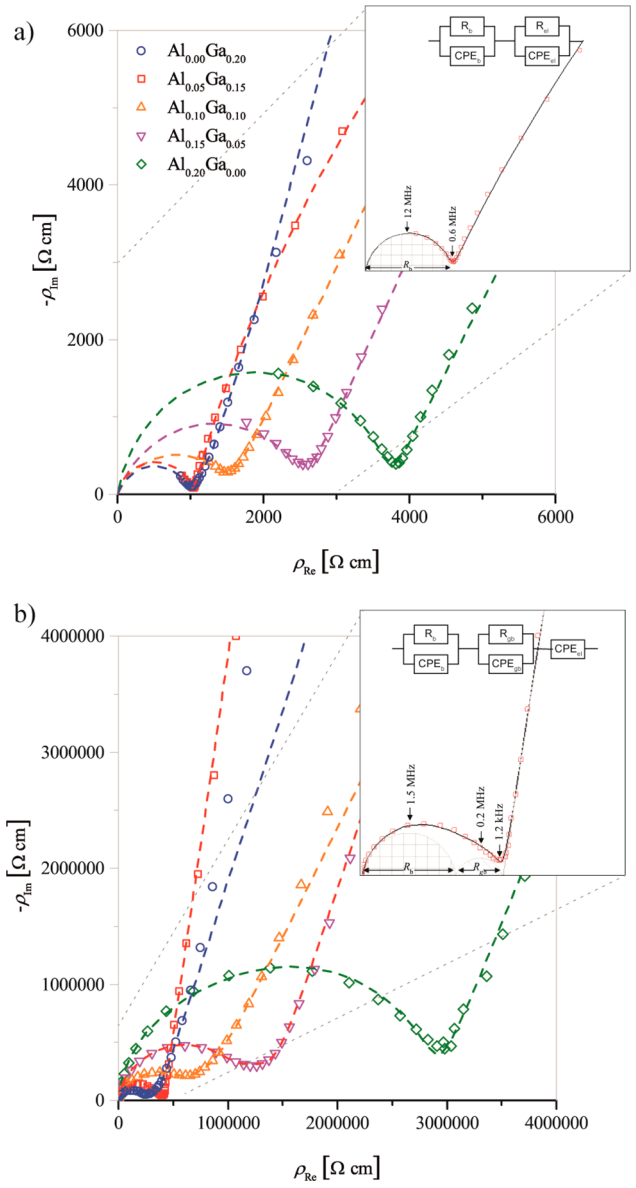

Figure 4. Impedance spectra of $Li_{6.4}Al_{0.2-x}Ga_xLa_3Zr_2O_{12}$ (x = 0.00, 0.05, 0.10, 0.15, and 0.20) samples at 20 °C (a), −80 °C (b), and dotted fit/simulation lines (equivalent circuit: R_b−CPE_b−R_{el}−CPE_{el}) are included. Data reflects resistivity ρ (normalized to the sample area and thickness).

the temperature decreases the high frequency arc becomes more apparent. The semiarcs can be fitted by a constant phase element (CPE_b) in parallel to a resistance element (R_b). The capacitance C_b calculated from the fit parameter Q_b and n ($C = (R^{1-n}Q)^{1/n}$) is in the pF range (refined from the equivalent circuit) and the calculated relative permittivity is about 40. Taken together these data suggest the high frequency arc is attributed to a bulk process.[29] The low frequency spike is well separated from the high (or intermediate arc at lower temperatures—see below) and can be attributed to the interface with electrodes. In a certain frequency range adding another R_{el}-CPE_{el} element (or CPE_{el} only at lower temperatures) improves the fit. This electrode equivalent circuit helps with analysis of the sample-specific high frequency features but does not imply any mechanistic information.

No indications of fast or resistive grain boundary contributions are observed at ambient temperatures. However, as the temperature decreased below −20 °C a slightly depressed semiarc at intermediate frequencies was observed in the plots. In some cases this intermediate arc could be fitted by another serial R_{gb}-CPE_{gb} element. Due to the large uncertainty in the capacitance C_{gb} of the intermediate arcs (10^{-9} to 10^{-11} F), the calculated thicknesses cannot be used to determine accurate normalized σ_{gb} values according to the brick-layer model.[30,31] The capacitance obtained represents grain boundary processes, and the corresponding activation energy can be calculated using the Arrhenius equation ($E_{a,gb}$ = 0.32(4) eV). The resulting equivalent circuits are shown in the inset of Figure 4; they fit all measurement data acceptably well (see dotted lines in Figure 4).

The temperature dependencies of σ_{bulk} (blocking electrodes) are shown in Figure 5 for all samples. The obtained σ_{bulk}, E_a,

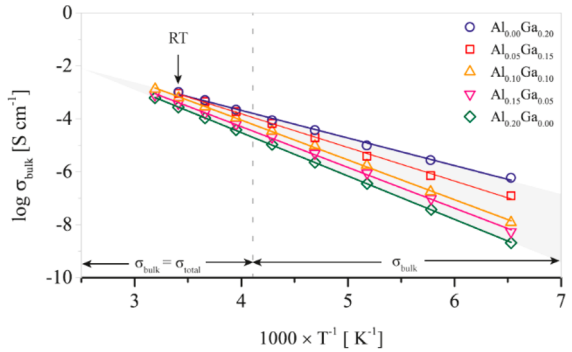

Figure 5. Temperature dependent bulk conductivities for $Li_{6.4}Al_{0.2-x}Ga_xLa_3Zr_2O_{12}$ (x = 0.00, 0.05, 0.10, 0.15 and 0.20). At ambient temperatures $\sigma_{bulk} = \sigma_{total}$.

Table 2. Li-Ion Conductivities, σ_{total}, Activation Energies, E_a, and Interfacial Area Specific Resistance, ASR, Measured by Using Blocking (Ti|Pt) and Ohmic (Li) Electrodes[a]

x	σ_{total} (Ti|Pt) [S cm^{-1}]	σ_{total} (Li) [S cm^{-1}]	E_a (Ti|Pt) [eV]	ASR (Li) [Ω cm^2]
0.00	2.63×10^{-4}	3.0×10^{-4}	0.314	77.8
0.05	3.80×10^{-4}	6.7×10^{-4}	0.282	27.8
0.10	6.30×10^{-4}	7.9×10^{-4}	0.281	25.2
0.15	1.06×10^{-3}	8.8×10^{-4}	0.264	24.4
0.20	1.18×10^{-3}	1.32×10^{-3}	0.256	24.2

[a]Accordingly, σ_{bulk} of Li ions in our LLZO samples was determined from R_b by using $\sigma_{bulk} = d/R_bA$.

and ASR values are given in Table 2. In order to determine the ASR as a function of the Al:Ga ratio, identically prepared samples of LLZO:$Al_{0.20-x}Ga_x$ sandwiched between Li electrodes were used. The corresponding impedance spectra are shown in Figure 6.

The Nyquist plots of cells containing LLZO:$Al_{0.20-X}Ga_x$, with x = 0.00, 0.05, 0.10, and 0.15 are composed of high frequency arcs, clearly visible intermediate frequency arcs, and a low frequency feature. As with the data obtained by fitting the spectra obtained on the cells with blocking electrodes, the high frequency arc was fitted by a R_b−CPE_b element for the cells containing samples with x = 0.00−0.15. In the case of LLZO with x = 0.20, due to the invisible high frequency arc, an R

DOI: 10.1021/acs.chemmater.6b00579
Chem. Mater. 2016, 28, 2384−2392

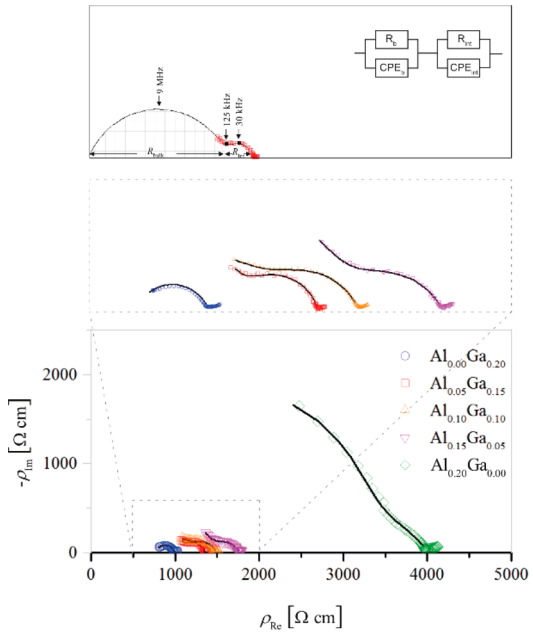

Figure 6. Impedance spectra of $Li_{6.4}Al_{0.2-x}Ga_xLa_3Zr_2O_{12}$ (x = 0.00, 0.05, 0.10, 0.15 and 0.20). For the sake of comparison, the data are normalized to the geometry ($\rho = RAd^{-1}$, with A = area and d = thickness). The bulk resistance clearly decreased with increasing Ga content. The solid lines represents the fit/simulation of LLZO:$Al_{0.20-X}Ga_x$, with x = 0.00, 0.05, 0.10, and 0.15 using the equivalent circuit shown in the inset. For sample $Al_{0.00}Ga_{0.20}$ the equivalent circuit without CPE_1 was used for fitting.

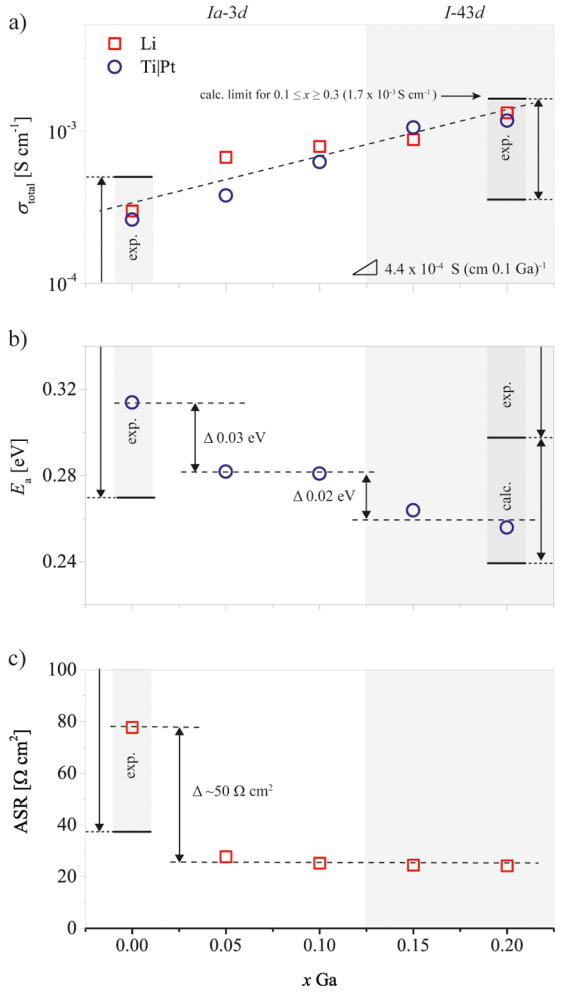

Figure 7. Activation energy (E_a) as a function of the Al:Ga portion in $Li_{6.4}Al_{0.2-x}Ga_xLa_3Zr_2O_{12}$ (x = 0.00, 0.05, 0.10, 0.15, and 0.20). A significant decrease in E_a for x = 0.05 and 0.15 can be observed. Dashed lines are included to guide the eye. The gray areas at x = 0.00 and 0.20 indicate values obtained from experiment (exp.) and calculations (calc.) from literature.

element only was used for the fitting procedure. The intermediate arc can be described by another R_{int}−CPE_{int} element. Since any intermediate arc can represent grain boundaries or the interface, we used the real capacitance calculated based on the CPE_{int} value to distinguish between these contributions. Since the CPE_{int} values are about 0.1 μF, typical of sample−electrode interface values, and no grain boundary contributions were observed at RT in the blocking electrode experiments, we can assign the intermediate arc to interface processes. The very small low frequency feature corresponds to an electrode response, which is typical for Li electrodes and will not be further considered in this study.[32,33] The resulting equivalent circuit used for all samples is displayed in the inset of Figure 6. This circuit fits the data well (solid line in Figure 6).

As shown in Figure 7a, the σ_{total} values (= σ_{bulk} above −20 °C) obtained by using blocking (blue circle) and ohmic (red squares) electrodes are in very good agreement and increase almost linearly as a function of the Ga content (slope 4.4 × 10^{-4} S cm^{-1}/0.1 Ga pfu). The σ_{total} values of LLZO:$Al_{0.20}Ga_{0.00}$ are very similar to values reported previously.[3,11−16] Significantly, the σ_{total} value of LLZO:$Al_{0.00}Ga_{0.20}$ is one of the highest values found for Li-oxide garnets.[17,34] Comparably high values were only reported by Bernuy-Lopez et al. as well as Li et al. for $Li_{6.4}Ga_{0.2}La_3Zr_2O_{12}$ (σ_{total} = 1.0 × 10^{-3} S cm^{-1} at 25 °C) and $Li_{6.4}La_3Zr_{1.4}Ta_{0.6}O_{12}$, ($\sigma_{total}$ = 1.3 × 10^{-3} S cm^{-1} at 25 °C), respectively (although the σ_{total} values of samples studied herein are measured at 20 °C).[17,35] The values are very close to the Li-ion conduction limit suggested by Jalem et al. on the basis of force field based simulations (σ_{bulk} = 1.7 × 10^{-3} S cm^{-1}).

In this study, no grain boundary contribution was observed above −20 °C. This finding is very similar to the observation reported by Tenhaeff et al. They have resolved the different contributions of Li-ion conduction in bulk and grain boundaries in hot pressed LLZO solid electrolytes and found that bulk resistance dominates at temperatures higher than −10 °C.[16] They also observed that the Li-ion conductivity in LLZO increases with decreasing grain size and increasing concentration of grain boundaries. These results suggest a relatively high grain boundary conductivity.[16]

As noted above, for σ_{total} (σ_{bulk} = σ_{total} at ambient temperatures), the increase from LLZO:$Al_{0.20}Ga_{0.00}$ to LLZO:$Al_{0.00}Ga_{0.20}$ (see Figure 7a) is almost linear, and no spontaneous increase in σ_{total}, e.g., caused by a phase transition, was observed. On the other hand, changes in activation energy of the samples in this study (see Figure 7b) show two distinct drops. LLZO:$Al_{0.20}Ga_{0.00}$ is characterized by an activation energy of 0.31 eV that is similar to values reported previously (about 0.26−0.37 eV).[3,12−16,32] With the incorporation of 0.05 Ga pfu into the LLZO structure (SG: $Ia\bar{3}d$) a significant decrease of E_a of about 0.03 eV was observed. A second drop in E_a of 0.02 eV was seen at x = 0.15. The E_a value of "end member" LLZO:$Al_{0.00}Ga_{0.20}$ is about 0.26 eV, which is lower

DOI: 10.1021/acs.chemmater.6b00579
Chem. Mater. 2016, 28, 2384−2392

than previously reported (0.30−0.37 eV)[17,36,37] but similar to computed values (0.24−0.30 eV).[38]

To understand the first drop in activation energy we calculated site energy differences using DFT. The migration pathway for Li-ion motion involves a series of transitions between tetrahedral and neighboring octahedral sites. The low energy sites are tetrahedral, but as the Li-ion concentration increases, the Li ions occupy the higher energy octahedral sites.[28] In order for the Li ion to migrate throughout the crystal structure, they must pass through the tetrahedral site located close to the supervalent cation.[38] We performed DFT calculations on structures with a single Al^{3+} or Ga^{3+} cation and a single Li^{+} with a compensating background charge and then computed the total energy difference in structures with the Li ion close to, or far from, the cation as shown in Figure 8a.

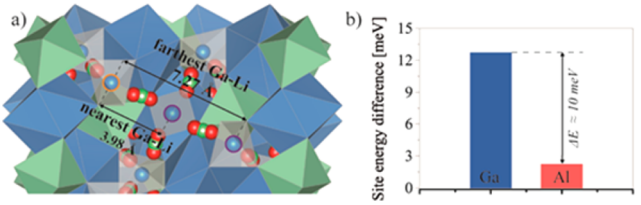

Figure 8. (a) $Ia\bar{3}d$ structures used for site energy difference calculations. The nearest and the farthest tetrahedral Ga−Li configuration is indicated. (b) Subtracting the difference of the total energy calculations for the nearest less the farthest configurations. It is evident that Al^{3+} is less repulsive than Ga^{3+}, and thus the Ga^{3+} acts to smooth the energy landscape more than Al^{3+}.

Our results indicate that Ga^{3+} raises the site energy of the neighboring tetrahedral site by 10 meV more than Al^{3+} (Figure 8b). In essence this increase in site energy acts to smooth the energy landscape by decreasing the site energy difference between the tetrahedral and octahedral sites. The rest of the improvement is likely associated with the increase in grain size and grains connectivity.

The second decrease in activation energy coincides with a phase change to SG $I\bar{4}3d$ at $x = 0.15$, similar to what was seen in recent NMR spectroscopy results of Ga stabilized LLZO with SG $I\bar{4}3d$.[18] In that study, an additional diffusion-induced relaxation rate peak in spin-lock ^{7}Li NMR experiments at low temperatures indicated a further diffusion process for LLZO stabilized with Ga ($x = 0.20$, SG: $I\bar{4}3d$), in contrast to samples stabilized with Al ($x = 0.00$, $Ia\bar{3}d$). Ab initio molecular dynamics support these findings showing more facile diffusion in the $I\bar{4}3d$ structure. Furthermore, the E_a values of Ga stabilized LLZO were slightly lower compared to Al stabilized LLZO.[18]

The area-specific resistance (ASR) of LLZO:$Al_{0.20}Ga_{0.00}$-containing cells turned out to be 77.8 Ω cm^{-1}, which is similar to values reported previously (see Figure 7c).[7,32,33,40−42] The lowest ASR value of 37 Ω cm^{-1} was recently obtained by Cheng et al. for cells containing samples with similar composition.[23,39] They found a strong correlation between the ASR and the microstructure of the LLZO solid electrolyte; in particular, the ASR was lower for samples in which the surfaces of the LLZO has a finer-grained microstructure and more grain boundaries. On the basis of this circumstance the higher ASR value obtained for LLZO:$Al_{0.20}Ga_{0.00}$ herein might be attributed to the larger average grain size of the sample. The trend observed in this study, in which ASR decreased for samples as Ga content rose, may be in part due to changes in the microstructure. There was a significant decrease in ASR of about 50 Ω cm^{-1} to values in the range of 24 to 28 Ω cm^{-1} for the samples containing Ga, the lowest reported values for LLZO solid electrolytes, as far as we know.

CONCLUSION

In summary, a phase transition from $Ia\bar{3}d$ to $I\bar{4}3d$ occurs with a critical amount of 0.15 Ga pfu in Ga and Al cosubstituted samples with general composition $Li_{6.4}Al_{0.2-x}Ga_xLa_3Zr_2O_{12}$ ($0 \leq x \leq 0.2$). The increase in Ga does not change the lattice parameter and the site distribution of substituent cations significantly but leads to a preference of the Li ions to occupy the 24*d* sites (or the equivalent sites in the $I\bar{4}3d$ structure). The change in structure coincides with an increase in the bulk Li-ion conductivity from 3.0×10^{-4} S cm^{-1} for 0 Ga pfu to 10^{-3} S cm^{-1} for 0.20 Ga pfu, with two significant drops in the activation energy at $x = 0.05$ and 0.15. DFT calculations show that the first drop in activation energy is largely related to Ga−Li repulsion, which acts to smooth the Li-ion diffusion energy landscape compared to Al; the second drop is due to the phase transition from $Ia\bar{3}d$ to $I\bar{4}3d$. This, combined with the changes in microstructure, seems to be the explanation for the almost linear increase in Li-ion conduction. An additional beneficial effect of the Ga substitution is a decrease in the interfacial resistance to values that are, to our knowledge, the lowest ever reported values of LLZO samples.

The success in making a dense LLZO sample with a Li-ion conductivity above 10^{-3} S cm^{-1} and an ASR of about 20 Ω cm^{-1} described in this work bodes well for the fabrication of devices with lithium anodes and LLZO solid electrolytes. The present study showed how important an in-depth understanding of the structure−property relationships in this class of materials is if we want to advance in developing new electrochemical energy storage devices.

AUTHOR INFORMATION

Corresponding Author

*(D.R.) E-mail: daniel.rettenwander@sbg.ac.at.

Author Contributions

The manuscript was written through contributions of all authors. All authors have given approval to the final version of the manuscript.

Funding

The research was supported by the Austrian Science Fund (FWF) project number P25702 and the Austrian Research Promotion Agency (FFG) SoLiK project. F.P.-P. and M.W. thank the Austrian Federal Ministry of Science, Research and Economy, and the National Foundation for Research, Technology and Development for financial support. We are grateful to ILL for making all facilities available.

Notes

The authors declare no competing financial interest.

REFERENCES

(1) Duduta, M.; Ho, B.; Wood, V. C.; Limthongkul, P.; Brunini, V. E.; Carter, W. C.; Chiang, Y.-M. Semi-Solid Lithium Rechargeable Flow Battery. *Adv. Energy Mater.* **2011**, *1*, 511−516.

(2) Visco, S. J.; Nimon, Y. S.; Katz, B. D. (Polyplus, USA). Protected Lithium Electrodes based on ceramic membranes. U.S. Patent 8,778,522, 2014.

DOI: 10.1021/acs.chemmater.6b00579
Chem. Mater. 2016, 28, 2384−2392

(3) Murugan, R.; Thangadurai, V.; Weppner, W. Fast lithium ion conduction in garnet-type $Li_7La_3Zr_2O_{12}$. *Angew. Chem., Int. Ed.* **2007**, *46*, 7778−7781.
(4) Thangadurai, V.; Narayanan, S.; Pinzaru, D. Garnet-type solid-state fast Li ion conductors for Li batteries: critical review. *Chem. Soc. Rev.* **2014**, *43*, 4714−4727.
(5) Awaka, J.; Takashima, A.; Hayakawa, H.; Kijima, N.; Idemoto, Y.; Akimoto, J. Single Crystal Synthesis of Cubic Garnet Related-type $Li_7La_3Zr_2O_{12}$ by a Self-Flux Method. *Key Eng. Mater.* **2011**, *485*, 99−102.
(6) Awaka, J.; Kijima, N.; Hayakawa, H.; Akimoto, J. Synthesis and structure analysis of tetragonal $Li_7La_3Zr_2O_{12}$ with the garnet-related type structure. *J. Solid State Chem.* **2009**, *182*, 2046−2052.
(7) Buschmann, H.; Dolle, J.; Berendts, S.; Kuhn, A.; Bottke, P.; Wilkening, M.; Heitjans, P.; Senyshyn, A.; Ehrenberg, H.; Lotnyk, A.; Duppel, V.; Kienle, L.; Janek, J. Structure and dynamics of the fast lithium ion conductor "$Li_7La_3Zr_2O_{12}$". *Phys. Chem. Chem. Phys.* **2011**, *13*, 19378−19392.
(8) Geiger, C. A.; Alekseev, E.; Lazic, B.; Fisch, M.; Armbruster, T.; Langner, R.; Fechtelkord, M.; Kim, N.; Pettke, T.; Weppner, W. Crystal Chemistry and Stability of "$Li_7La_3Zr_2O_{12}$" Garnet: A Fast Lithium-Ion Conductor. *Inorg. Chem.* **2011**, *50* (3), 1089−1097.
(9) Wolfenstine, J.; Ratchford, J.; Rangasamy, E.; Sakamoto, J.; Allen, J. L. Synthesis and high Li-ion conductivity of Ga-stabilized cubic $Li_7La_3Zr_2O_{12}$. *Mater. Chem. Phys.* **2012**, *134*, 571−575.
(10) Rettenwander, D.; Langer, J.; Schmidt, W.; Arrer, C.; Harris, K. J.; Terskikh, V.; Goward, G. R.; Wilkening, M.; Amthauer, G. Site Occupation of Ga and Al in Stabilized Cubic $Li_{7-3(x+y)}Ga_xAl_yLa_3Zr_2O_{12}$ Garnets As Deduced from ^{27}AI and ^{71}Ga MAS NMR at Ultrahigh Magnetic Fields. *Chem. Mater.* **2015**, *27*, 3135−3142.
(11) Cheng, L.; Park, J. S.; Hou, H. M.; Zorba, V.; Chen, G. Y.; Richardson, T.; Cabana, J.; Russo, R.; Doeff, M. Effect of microstructure and surface impurity segregation on the electrical and electrochemical properties of dense Al-substituted $Li_7La_3Zr_2O_{12}$. *J. Mater. Chem. A* **2014**, *2*, 172−181.
(12) Shimonishi, Y.; Toda, A.; Zhang, T.; Hirano, A.; Imanishi, N.; Yamamoto, O.; Takeda, Y. Synthesis of garnet-type $Li_{7-x}La_3Zr_2O_{12-1/2x}$ and its stability in aqueous solutions. *Solid State Ionics* **2011**, *183*, 48−53.
(13) Rangasamy, E.; Wolfenstine, J.; Sakamoto, J. The role of Al and Li concentration on the formation of cubic garnet solid electrolyte of nominal composition $Li_7La_3Zr_2O_{12}$. *Solid State Ionics* **2012**, *206*, 28−32.
(14) Zhang, Y. H.; Chen, F.; Tu, R.; Shen, Q.; Zhang, L. M. Field assisted sintering of dense Al-substituted cubic phase $Li_7La_3Zr_2O_{12}$ solid electrolytes. *J. Power Sources* **2014**, *268*, 960−964.
(15) Jin, Y.; McGinn, P. Al-doped $Li_7La_3Zr_2O_{12}$ synthesized by a polymerized complex method. *J. Power Sources* **2011**, *196*, 8683−8687.
(16) Tenhaeff, W. E.; Rangasamy, E.; Wang, Y. Y.; Sokolov, A. P.; Wolfenstine, J.; Sakamoto, J.; Dudney, N. J. Resolving the Grain Boundary and Lattice Impedance of Hot-Pressed $Li_7La_3Zr_2O_{12}$ Garnet Electrolytes. *ChemElectroChem* **2014**, *1*, 375−378.
(17) Bernuy-Lopez, C.; Manalastas, W.; Lopez del Amo, J. M.; Aguadero, A.; Aguesse, F.; Kilner, J. A. Atmosphere Controlled Processing of Ga-Substituted Garnets for High Li-Ion Conductivity Ceramics. *Chem. Mater.* **2014**, *26*, 3610−3617.
(18) Wagner, R.; Redhammer, G. J.; Rettenwander, D.; Senyshyn, A.; Schmidt, W.; Wilkening, M.; Amthauer, G. Crystal structure of garnet-related Li-ion conductor $Li_{7-3x}Ga_xLa_3Zr_2O_{12}$: Fast Li-ion conduction caused by a different cubic modification? *Chem. Mater.* **2016**, DOI: 10.1021/acs.chemmater.6b00038.
(19) Bruker *APEX2*, Bruker AXS Inc., Madison, Wisconsin, USA, 2012.
(20) Sheldrick, G. M. A short history of SHELX. *Acta Crystallogr., Sect. A: Found. Crystallogr.* **2008**, *64*, 112−122.
(21) Farrugia, L. J. WinGX and ORTEP for Windows: an update. *J. Appl. Crystallogr.* **2012**, *45*, 849−854.
(22) Rettenwander, D.; Amthauer, G.; Redhammer, G.; Suard, E.; Wagner, R. Neutron Powder Diffraction Study on Al and Ga in Mixed Doped $Li_{5.8}Ga_{0.4-x}Al_xLa_3Zr_2O_{12}$ Garnet Solid Solutions with x = 0.00−0.40. *Institut Laue-Langevin (ILL)*. DOI: 10.5291/ILL-DATA.5-22-735.
(23) Cheng, L.; Chen, W.; Kunz, M.; Persson, K.; Tamura, N.; Chen, G.; Doeff, M. Effect of surface microstructure on electrochemical performance of garnet solid electrolytes. *ACS Appl. Mater. Interfaces* **2015**, *7*, 2073−81.
(24) Ong, S. P.; Richards, W. D.; Jain, A.; Hautier, G.; Kocher, M.; Cholia, S.; Gunter, D.; Chevrier, V. L.; Persson, K. A.; Ceder, G. Python Materials Genomics (pymatgen): A robust, open-source python library for materials analysis. *Comput. Mater. Sci.* **2013**, *68*, 314−319.
(25) Perdew, J. P.; Ernzerhof, M.; Burke, K. Rationale for mixing exact exchange with density functional approximations. *J. Chem. Phys.* **1996**, *105*, 9982.
(26) Kresse, G.; Furthmüller, J. Efficient iterative schemes forab initiototal-energy calculations using a plane-wave basis set. *Phys. Rev. B: Condens. Matter Mater. Phys.* **1996**, *54*, 11169−11186.
(27) Blöchl, P. E. Projector augmented-wave method. *Phys. Rev. B: Condens. Matter Mater. Phys.* **1994**, *50*, 17953−17979.
(28) Xu, M.; Park, M. S.; Lee, J. M.; Kim, T. Y.; Park, Y. S.; Ma, E. Mechanisms of Li^+ transport in garnet-type cubic $Li_{3+x}La_3M_2O_{12}$ (M = Te, Nb, Zr). *Phys. Rev. B: Condens. Matter Mater. Phys.* **2012**, *85*, 052301.
(29) Rettenwander, D..; Cheng, L.; Fleig, J.; Musso, M.; Suard, E.; Doeff, M. M.; Redhammer, G. J.; Amthauer, G.; Welzl, A. Synthesis, Crystal Chemistry, and Electrochemical Properties of $Li_{7-2x}La_3Zr_{2-x}Mo_xO_{12}$ (x = 0.1−0.4): Stabilization of the Cubic GarnetPolymorph via Substitution of Zr^{4+} by Mo^{6+}. *Inorg. Chem.* **2015**, *54*, 10440−10449.
(30) Maier, J. On the conductivity of polycrystalline materials. *Ber. Bunsenges. Phys. Chem.* **1986**, *90*, 26−33.
(31) Fleig, J. The grain boundary impedance of random microstructures: numerical simulations and implications for the analysis of experimental data. *Solid State Ionics* **2002**, *150*, 181−193.
(32) Cheng, L.; Crumlin, E. J.; Chen, W.; Qiao, R.; Hou, H.; Franz Lux, S.; Zorba, V.; Russo, R.; Kostecki, R.; Liu, Z.; Persson, K.; Yang, W.; Cabana, J.; Richardson, T.; Chen, G.; Doeff, M. The origin of high electrolyte-electrode interfacial resistances in lithium cells containing garnet type solid electrolytes. *Phys. Chem. Chem. Phys.* **2014**, *16*, 18294−300.
(33) Buschmann, H.; Berendts, S.; Mogwitz, B.; Janek, J. Lithium metal electrode kinetics and ionic conductivity of the solid lithium ion conductors "$Li_7La_3Zr_2O_{12}$" and $Li_{7-x}La_3Zr_{2-x}Ta_xO12$ with garnet-type structure. *J. Power Sources* **2012**, *206*, 236−244.
(34) Li, Y. T.; Han, J. T.; Wang, C. A.; Xie, H.; Goodenough, J. B. Optimizing Li^+ conductivity in a garnet framework. *J. Mater. Chem.* **2012**, *22*, 15357−15361.
(35) Li, Y. T.; Han, J. T.; Wang, C. A.; Vogel, S. C.; Xie, H.; Xu, M. W.; Goodenough, J. B. Ionic distribution and conductivity in lithium garnet $Li_7La_3Zr_2O_{12}$. *J. Power Sources* **2012**, *209*, 278−281.
(36) El Shinawi, H.; Janek, J. Stabilization-of cubic lithium-stuffed garnets of the type "$Li_7La_3Zr_2O_{12}$" by addition of gallium. *J. Power Sources* **2013**, *225*, 13−19.
(37) Afyon, S.; Krumeich, F.; Rupp, J. L. M. A shortcut to garnet-type fast Li-ion conductors for all-solid state batteries. *J. Mater. Chem. A* **2015**, *3*, 18636−18648.
(38) Jalem, R.; Rushton, M. J. D.; Manalastas, W.; Nakayama, M.; Kasuga, T.; Kilner, J. A.; Grimes, R. W. Effects of Gallium Doping in Garnet-Type $Li_7La_3Zr_2O_{12}$ Solid Electrolytes. *Chem. Mater.* **2015**, *27* (8), 2821−2831.
(39) Cheng, L.; Wu, C. H.; Jarry, A.; Chen, W.; Ye, Y. F.; Zhu, J. F.; Kostecki, R.; Persson, K.; Guo, J. H.; Salmeron, M.; Chen, G. Y.; Doeff, M. Interrelationships among Grain Size, Surface Composition, Air Stability, and Interfacial Resistance of Al-Substituted $Li_7La_3Zr_2O_{12}$ Solid Electrolytes. *ACS Appl. Mater. Interfaces* **2015**, *7*, 17649−17655.
(40) Rangasamy, E.; Sahu, G.; Keum, J. K.; Rondinone, A. J.; Liang, C.; Dudney, N. J. A high conductivity oxide−sulfide composite lithium superionic conductor. *J. Mater. Chem. A* **2014**, *2*, 4111−4116.

DOI: 10.1021/acs.chemmater.6b00579
Chem. Mater. 2016, 28, 2384−2392

(41) Ishiguro, K.; Nemori, H.; Sunahiro, S.; Nakata, Y.; Sudo, R.; Matsui, M.; Takeda, Y.; Yamamoto, O.; Imanishi, N. Ta-Doped $Li_7La_3Zr_2O_{12}$ for Water-Stable Lithium Electrode of Lithium-Air Batteries. *J. Electrochem. Soc.* **2014**, *161*, A668−A674.
(42) Ishiguro, K.; Nakata, Y.; Matsui, M.; Uechi, I.; Takeda, Y.; Yamamoto, O.; Imanishi, N. Stability of Nb-Doped Cubic $Li_7La_3Zr_2O_{12}$ with Lithium Metal. *J. Electrochem. Soc.* **2013**, *160*, A1690−A1693.

DOI: 10.1021/acs.chemmater.6b00579
Chem. Mater. 2016, 28, 2384−2392